Revista Brasileira de Ciências Ambientais
Brazilian Journal of Environmental Sciences

Carbon monoxide profile variability over the Manaus Metropolitan Region and its relations with biomass burning

Variabilidade do perfil vertical de monóxido de carbono sobre a Região Metropolitana de Manaus e sua relação com a queima de biomassa

Renato Trevisan Signori[1], *Rodrigo Augusto Ferreira de Souza*[2], *Rita Valeria Andreoli de Souza*[2], *Igor Oliveira Ribeiro*[2], *Mary Toshie Kayano*[3]

ABSTRACT

The present study analyzes the temporal variability of carbon monoxide (CO) over the Manaus Metropolitan Region (MMR) and its relations with nearby fires based on data obtained by the environmental satellite AQUA, for the 2003–2020 period. For this purpose, wavelet transform analyses and wavelet coherence analyses were used. The results show a well-defined seasonal behavior, with an increase and decrease in mean CO concentrations during dry and wet seasons, respectively. Semiannual and annual scales represent around 95 % of CO temporal variability in lower troposphere (500 to 1,000 hPa) and are associated with rains and fires dynamics in the region. In terms of interannual variability, multiple variability scales (1.2–2, 2.5–3 and 4.5–6 years) were observed, which explain around 10–15 % of concentration variability near surface. The results suggest that climatic variations, associated with the tropical Pacific and Atlantic sea surface temperature variations, on these different time scales, affect rain dynamics and, consequently, fires and CO concentration. Specifically, in 2015/16, the combined effect from different variability scales acted to prolong the dry period over the region, which contributed to increase fires and the CO to reach higher values compared to previous years. These results show a new aspect of the importance of evaluating the combined effect of different climate variability scales on CO concentrations in the atmosphere.

Keywords: carbon monoxide; fires; climate variability; Amazon; remote sensing; wavelet transform.

RESUMO

O presente estudo analisa a variabilidade temporal do gás monóxido de carbono (CO) sobre a Região Metropolitana de Manaus (RMM) e sua relação com as queimadas com base em informações obtidas pelo satélite ambiental AQUA, para o período entre 2003 e 2020. Para tal, foram realizadas análises de transformada de ondeleta e análises de coerência e fase da ondeleta. Os resultados apontam para um comportamento sazonal bem definido, com aumento das concentrações médias de CO durante a estação seca e redução na estação chuvosa. As escalas semianual e anual representam cerca de 95% da variabilidade temporal do CO na baixa troposfera (500 a 1.000 hPa) e estão associadas à dinâmica das chuvas e queimadas na região. Com relação à variabilidade interanual, observaram-se múltiplas escalas de variabilidade (1,2–2, 2,5–3 e 4,5–6 anos), que explicam juntas em torno de 10–15 % da variabilidade das concentrações próximas à superfície. Os resultados sugerem que variações climáticas, associadas às variações da temperatura da superfície do mar nos oceanos Pacífico e Atlântico tropicais, nessas diferentes escalas de tempo, afetam a dinâmica das chuvas e, consequentemente, as queimadas e a concentração de CO. Especificamente em 2015/16, o efeito combinado das diferentes escalas de variabilidade atuou para prolongar o período seco sobre a região, o que contribuiu para o aumento das queimadas e para que o CO alcançasse maiores valores em relação aos anos anteriores. Tais resultados mostram um aspecto novo sobre a importância de avaliar o efeito combinado de diferentes escalas de variabilidade climática nas concentrações de CO na atmosfera, particularmente em anos extremos.

Palavras-chave: monóxido de carbono; queimadas; variabilidade climática; Amazônia; sensoriamento remoto; transformada de ondeleta.

[1]Instituto Nacional de Pesquisas da Amazônia – Manaus (AM), Brazil.

[2]Universidade do Estado do Amazonas – Manaus (AM), Brazil.

[3]Instituto Nacional de Pesquisas Espaciais – São José dos Campos (SP), Brazil.

Correspondence address: Renato Trevisan Signori – Universidade do Estado do Amazonas, Instituto Nacional de Pesquisas da Amazônia, Postgraduate Program in Climate and Environment – Avenida André Araújo, 2936 – Campus II, Aleixo – CEP: 69060-001 – Manaus (AM), Brazil.

E-mail: renato.tsignori@gmail.com

Conflicts of interest: the authors declare that there are no conflicts of interest.

Funding: Coordenação de Aperfeiçoamento de Pessoal de Nível Superior – Brasil (CAPES) – Finance Code 001; National Council for Scientific and Technological Development (CNPq), grant 308435/2022-2.

Received on: 01/09/2023. Accepted on: 06/01/2023.

https://doi.org/10.5327/Z2176-94781534

Introduction

Carbon monoxide (CO) is a colorless, tasteless and odorless gas, dangerous to human health due to its toxicity and capacity to promote chemical asphyxiation (Rozante et al., 2017). CO has both anthropogenic and natural sources, with anthropogenic emissions being responsible for more than half of the total CO injected into the atmosphere (Petrenko et al., 2013). On the other hand, the main CO sink is its reaction with hydroxyl radical (OH), with CO consuming between 39 and 60% of OH in troposphere (Seiler et al., 1984; Lelieveld et al., 2016), being its major oxidizing agent (Logan et al., 1981). The CO atmospheric balance and the reduction of OH concentrations are also directly related to the residence time of other gases in the atmosphere, including methane (CH_4) and sulfur dioxide (SO_2). Furthermore, CO is an important precursor of the tropospheric ozone (O_3) and carbon dioxide (CO_2), which are pollutants present in the lower layers of the atmosphere (Shindell et al., 2009; Strode et al., 2015; Zheng et al., 2019). Thus, although CO is not considered a primary greenhouse gas, it can play a significant role in determining temperature trends.

During its lifetime in troposphere (about two months), CO can be used as a tracer for monitoring atmospheric transport processes and identifying pollution sources of both natural and human origin. Due to its non-uniform mixing within the troposphere, CO can be measured with high precision and accuracy, enabling effective analysis and detection (Logan et al., 1981; Boian and Kirchhoff, 2004; Kopacz et al., 2010; Zhang et al., 2016). Such characteristics allow the gas to be used as a human activities' indicator since the main CO sources had anthropogenic origins (Worden et al., 2010; Hooghiemstra et al., 2012; Davidson et al., 2012). Therefore, to correctly interpret observed CO variations, it is important to assess worldwide CO sources contributions (Yashiro et al., 2009).

In the Amazon, the concentration of CO in the atmosphere increases during the dry seasons, in response to increases in biomass burning (Ribeiro et al., 2018b). In addition to these seasonal variations, CO concentrations in tropical atmosphere show an interannual variability correlated with variations in biomass burning and large-scale climatic phenomenon (Novelli et al., 2003; Liu et al., 2013). Recently, adoption of public and economic policies that aim at a broader use of natural resources in the region, intensifying geographic expansion and food production, as well as the recent loosening of forest protection policies, linked soil use to the practice of deforestation and fire use. In this scenario, CO variability in the Amazon Basin results primarily from fires associated with deforestation (Langenfelds et al., 2002; Novelli et al., 2003; Deeter et al., 2016). Deeter et al. (2018) claim that the maximum CO concentrations in lower troposphere are observed in southwest Amazon Basin in August and September due to the transport of pollutants from the "Arc of Deforestation" region, where, after deforestation process, fires are often used to remove biomass, to prevent trees from encroaching on pastures, to recycle nutrients and to remove crop residues. Human-induced fires in tropical forests, each year, surpass the importance of natural fires (van der Werf et al., 2010). In addition, the occurrence of biomass burning increases during years that are considered dry. The 2015 drought was considered the most extreme since 1901 (Erfanian et al., 2017) and is possibly the first that has been linked to the increase in biomass burning in areas that are rarely affected by fires, such as the central Amazon (Ribeiro et al, 2018b).

El Niño-Southern Oscillation (ENSO) and the tropical north Atlantic Sea Surface Temperature (SST) variations have been considered the main factors that explain the interannual precipitation variability over the Amazon Basin (Marengo et al., 2008b; Davidson et al., 2012; Panisset et al., 2018). Such phenomena were responsible for intense drought episodes in 2005 (Marengo et al., 2008a, 2008b); 2010 (Marengo et al., 2011) and 2015–2016 (Jiménez-Muñoz et al., 2016; Erfanian et al., 2017), leading to higher frequency of the forest fires during these extremely dry years, which in turn have impacts on interannual variability of CO and CH_4 in the region (Aragão et al., 2018). Thus, the monitoring of CO source changes and its subsequent transport is crucial to predicting its impact on tropospheric chemistry and surface air quality (McMillan et al., 2011). However, atmospheric CO monitoring has not been as prolonged or extensive as for CO_2 (Langenfelds et al., 2002). Therefore, to understand how fires influence and interact with the atmosphere, quantitative information about emissions and their different sources is needed (van Marle et al., 2017). In the face of polluting gas emissions and analysis of the impact of human activities in the context of climate change, satellite remote sensing is one of the most important methods for monitoring atmospheric parameters and their changes, providing global coverage and data with good temporal and spatial resolution, being able to detecting pollution sources and propagation patterns that conventionally are been difficult to measure due to high costs. Atmospheric Infrared Sounder (AIRS) on the board of the EOS/AQUA satellite has the advantages of wide spatial coverage with time continuity, which significantly contributes to studies of remote areas such as the Amazon, as demonstrated by Kopacz et al. (2010), Zhang et al. (2016), Santos et al. (2017), Ribeiro et al. (2018a, 2018b, 2020). Therefore, the purpose of this study was to investigate the temporal variability of the CO vertical profile over the Manaus Metropolitan Region (MMR), to evaluate the relationships between its variability and the fires and precipitation variability, using wavelet transform and wavelet coherence transform applied to 18 years of data obtained by the NASA/AQUA satellite.

Methodology

Study area

The study area covers the MMR, which comprises the cities of Autazes, Careiro, Careiro da Várzea, Iranduba, Itacoatiara, Itapiranga, Manacapuru, Manaquiri, Manaus (capital), Novo Airão, Presidente Figueiredo, Rio Preto da Eva and Silves (Figure 1). The MMR includes the Manaus Industrial Pole, which holds industries from different segments and important technological and research centers. According to Fórum Nacional de Entidades Metropolitanas (FNEM, 2018), the total number of inhabitants in this region is around 2,630,000 and its territorial extension is of 101,401 km², approximately. It is characterized by lowlands, low plateaus and "terra firme" forests, with an average altitude lower than 100 meters.

Data source

AIRS data are available from National Aeronautics and Space Administration (NASA) Goddard Earth Sciences Data and Information Services Center (DISC). The monthly CO vertical profile (L3 AIRS3STD product, version 7) data were obtained from the AIRS sensor on-board the AQUA satellite for the 2003–2020 period. This dataset has coverage in grid points with horizontal resolution of 1º (longitude and latitude) and temporal resolution of two daily passes, with vertical CO concentrations arranged in 24 pressure levels (from 1,000 to 1 hPa). Information from the Burning Database was also used, referring to daily biomass burning for the 2003–2020 period, available on the electronic portal of the National Institute for Space Research (INPE, 2022). Precipitation data from the Climate Hazards Group InfraRed Precipitation with Station Data CHIRPS (Funk et al., 2014; Funk et al., 2015) version v2.0, developed by the Earth Resources Observation and Science Center of the U.S. Geological Survey and the Climate Risk Group at the University of California, Santa Barbara, were used. This dataset is available on the Climate Hazards Center website and for the purposes of this study, a spatial resolution of 0.25º and a temporal resolution of one month were used. Thus, monthly precipitation data for the period from 2003 to 2019 were obtained over the Legal Amazon region. Sea Surface Temperature (SST) data were obtained from the reconstructed dataset of version 5 provided by the National Oceanic and Atmospheric Administration (NOAA, 2022).

Methods

In order to investigate the CO concentration temporal evolution at different pressure levels, a pressure *versus* time diagram of the monthly CO concentration and its deviations in relation to the climatology over MMR is presented. The climatology was obtained considering the monthly average of the period 2003–2020, and deviations represent the difference between the observed values of a variable in each month and their monthly climatologic value. To simplify, the deviations are referred to as anomalies hereafter. Then, the time-frequency variability of CO concentrations and CO anomaly time series were obtained through wavelet analyses. The time-frequency analysis was performed using the Morlet wavelet. This function is a complex exponential modulated by a Gaussian $\psi_0(n) = \pi^{-1/4} e^{i\omega_0\eta} e^{-\eta^2/2}$, where $\eta = t/s$, t is the time, S is the wavelet scale and ω_0 is the non-dimensional frequency, for which the value of 6 is used (Torrence and Compo, 1998). As a result, wavelet power spectrum is obtained, which is defined as the square of the absolute value of the wavelet transform coefficient, which provides measure of the variance of the time series at each scale and time, where the real part of the wavelet coefficients gives a strength and phase description signal at a given time and scale, in relation to other times and scales (Weng and Lau, 1994).

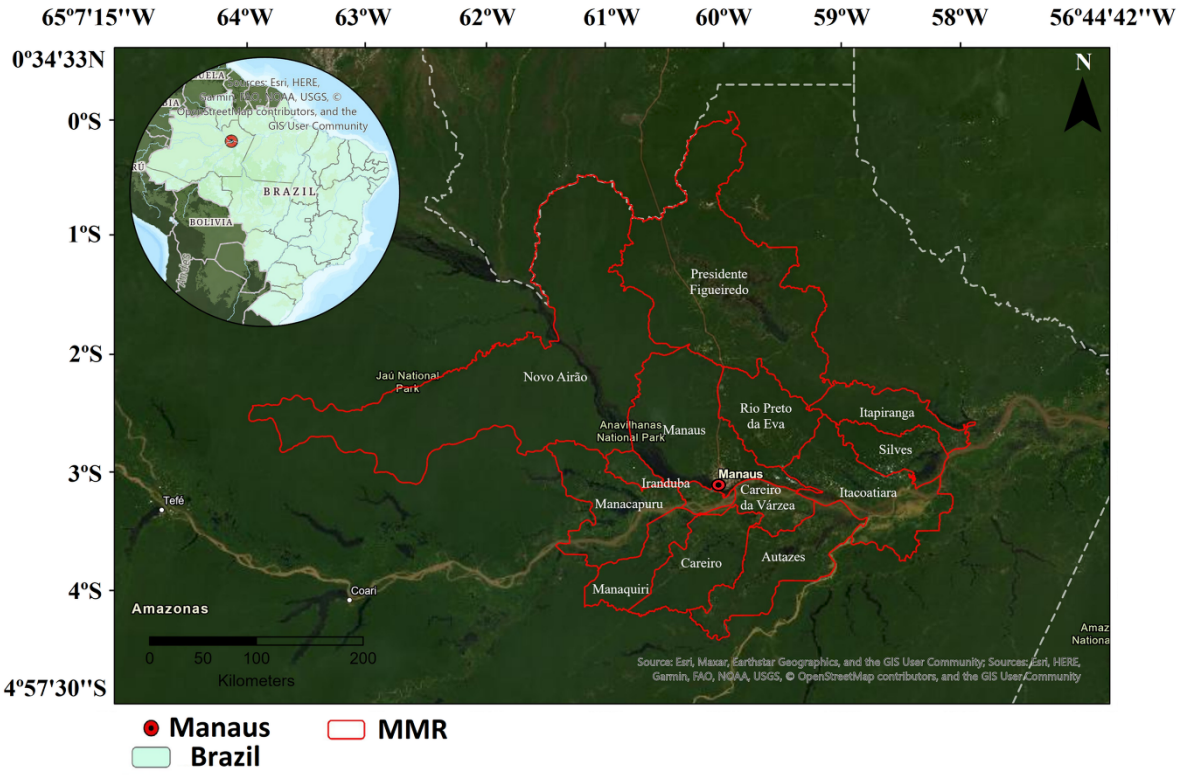

Figure 1 – Cities of Manaus Metropolitan Region.

Thus, it was possible to transform a one-dimensional time series into a time-frequency space, which allows the dominant variability scales determination and their temporal variations. The next step was to decompose the time series on the selected time scales. The wavelet transform was then used as a band-pass filter, with the average wavelet power per scale $\bar{W}$, being defined as the weighted sum of the wavelet power spectrum from scale s1 to s2, given by Equation 1:

$$\bar{W}^2_n = \frac{\delta j \delta t}{C_\delta} \cdot \sum_{j=j1}^{j2} \cdot \frac{\left|W_n(S_j)^2\right|}{S_j} \quad (1)$$

Where:
$W_n(S_j)$: the wavelet coefficient at levels n and S_j;
C_δ: a constant reconstruction factor and comes from δ as a function of its wavelet transform using $\psi_0(n)$, while the average per scale of the wavelet real part coefficients $R[W_n(S_j)]$ is given by Equation 2:

$$x'_n = \frac{\delta_j \delta_t{}^{1/2}}{C_\delta \psi_0(0)} \cdot \sum_{j=j1}^{j2} \cdot \frac{R[W_n(S_j)]}{s_j^{1/2}} \quad (2)$$

Where:
$\psi_0(0) = \pi^{-1/4}$ is a factor that removes the energy scaling;
$S_j^{1/2}$ converts the wavelet transform into an energy density.

Time scales s1 and s2 were selected based on the identification of the dominant variability scales contained in the monthly CO and CO anomaly time series.

Relations between CO and fires anomalies were evaluated using the wavelet cross-spectrum (XWT), wavelet coherence (WTC) and phase differences, following the methodology described by Torrence and Webster (1999) and Grinsted et al. (2004). The cross-wavelet highlights coincident energy regions between two signals, in addition to determining the relative phase between both (Vale et al., 2020). It is determined by multiplying the first complex wavelet with the second one's complex conjugate (Equation 3):

$$W_n^{XY}(s) = W_n^X(s) W_n^{Y*}(s) \quad (3)$$

Where:
X and Y: the time series;
n: the time;
S: the wavelet scale;
*the complex conjugate (Torrence and Webster, 1999).

Cross-wavelet is complex, so it is possible to define its spectrum as $W_n^x(s)^2$. The transform displays the covariance between X and Y and reveals information about the relation between the series phases; in this way, the XWT quantitatively indicates the power similarity between series. Phase difference analysis between series provides a better characterization of the relationship between them.

Specifically, the WTC analysis and the phase difference of the wavelets is used to quantify linear relationship between two non-stationary time series on time and frequency domains. The WTC reveals the correlation degree between both series in a time and frequency, thus explaining how much a variability of one series is justified by another series of data. According to Torrence and Webster (1999), the square of coherence in wavelet is defined as the square of the absolute value of the smoothed XWT, normalized by the wavelet power spectrum (Equation 4),

$$R_n^2(s) = \frac{|\langle s^{-1} W_n^{XY}(s)\rangle|^2}{\langle s^{-1}|W_n^X(s)|^2\rangle \langle s^{-1}|W_n^Y(s)|^2\rangle} \quad (4)$$

Where:
(.): a smoothing operator in both time and scale.

The numerator has both imaginary and real parts of the continuous wavelet transform being smoothed separately before assuming an absolute value. On the other hand, the denominator has the wavelet power spectrum (after being squared) and then smoothed. The factor S^{-1} is used to transform in energy density. From these definitions we have that $R_n^2(s)$ variates between 0 and 1, with 0 indicating no correlation between the two series, and 1, a perfect correlation. The statistical significance of the wavelet analysis and wavelet coherence is performed using the Monte Carlo methods, following Torrence and Webster (1999) and Grinsted et al. (2004).

To assign a support value to the phase difference measurements between two data series, the wavelet phase coherence calculation is performed. The phase coherence of the wavelet can be defined by Equation 5:

$$\phi_n(s) = tan^{-1} \cdot \frac{I\{\langle s^{-1} W_n^{XY}(s)\rangle\}}{R\{\langle s^{-1} W_n^{XY}(s)\rangle\}} \quad (5)$$

with *R* indicating the real part and *I* the imaginary part of the function, both smoothed, and could already be calculated in Equation 3. Both $R_n^2(s)$ and $\phi_n(S)$ are functions of time index n and scale s. The smoothing performed in Equation 4 is performed using convolution in the time direction and scale.

Finally, the relationship between the multiscale variability of CO and the precipitation variability during the period 2015–2016 was investigated. This period was characterized by an intense and long drought over the study region. So, the series of precipitation anomalies over the Legal Amazon and the SST over the tropical oceans were reconstructed at different time scales to determine seasonal patterns by scales that contributed to the increase of fires in the region and, consequently, to the increase in CO emissions between July of 2015 and March of 2016.

Results and Discussion

Temporal evolution of the carbon monoxide concentrations and their variability over the Manaus Metropolitan Region

Figure 2A presents the pressure *versus* time diagram of the time series of the monthly profiles from 2003 to 2020. It is possible to note a well-defined seasonal behavior of CO concentrations, with highest values during the dry season of the region, consistent with previous results (Deeter et al., 2016; Santos et al., 2017; Ribeiro et al., 2018a). In addition, the CO concentration presents interannual variability, with the highest concentration in the years 2004–2005, 2006–2007, 2009–2010 and 2015–2016. Interannual variations on CO concentration are better visualized analyzing the pressure *versus* time diagram of the CO concentrations anomaly time series over the MMR (Figure 2B). It is observed in this figure that the years of 2004, 2005, 2007, 2010 e 2015 present largest positive anomalies, while 2011, 2013, 2014 e 2018 show negative anomalies. In addition, the interannual variability of CO over the MMR is related to the ENSO, such that the years of greater positive anomalies coincide with the occurrence of El Niño episodes, while in the years 2013 and 2018, there were La Niña episodes instead (NOAA, 2022).

These results are consistent with the previous findings that explained the increase in the total CO column in terms of the fire activity that was associated with the extremely dry years during El Niño (Santos et al., 2017; Aragão et al., 2018; Ribeiro et al., 2018a). According to Aragão et al. (2018), interannual climate variability plays a role in regulating fires in the Amazon, which, in turn, have considerable impacts on the CO concentrations in the region. In addition, Ribeiro et al. (2020) show that the number of biomass burning events increased significantly during the El Niño in 2015–16 when compared to the average number from 2003 to 2016. Consequently, the total CO column concentration values in the MMR increased by 15% when compared to the normal conditions, indicating that the impacts of biomass burning were exacerbated during the strong El Niño event as compared to the non-El Niño period.

Figure 3A presents the time-frequency variations of the monthly CO time series at 500 hPa and 1,000 hPa levels over MMR obtained from wavelet analyses. At both levels there were two dominant variability periods: the annual cycle, from 0.7 to 1.2 year, and semiannual from 0.4 to 0.7 year. Locally, the semiannual scale shows significant values in the 2005–06, 2007–09 and 2010–11 years, while on the annual scale values are significant throughout the entire period. These results remain along the different pressure levels, with small changes in the percentage of annual or semiannual variance in relation to the total variance of the series, as shown in Figure 3B. In this figure, the normalized profiles were expressed in terms to the percentage of the total variance that each variability band (annual or semiannual) represents. Thus, it is possible to identify that, for the CO concentration time series, the semiannual scale explains about of 12 to 18% of the CO variability at surface levels. Between 500 and 100 hPa levels, the variance values were between 15.5 and 17.5%, approximately. The annual scale represents of the order of 58 and 74% of the CO variability at surface levels and approximately 65–70% between 500 and 100 hPa levels. Such results reinforce the seasonal behavior of CO concentration throughout the year as a function of two well-defined scales, which represent around 95% of total CO concentration variability at surface levels and approximately 90% at 500 hPa.

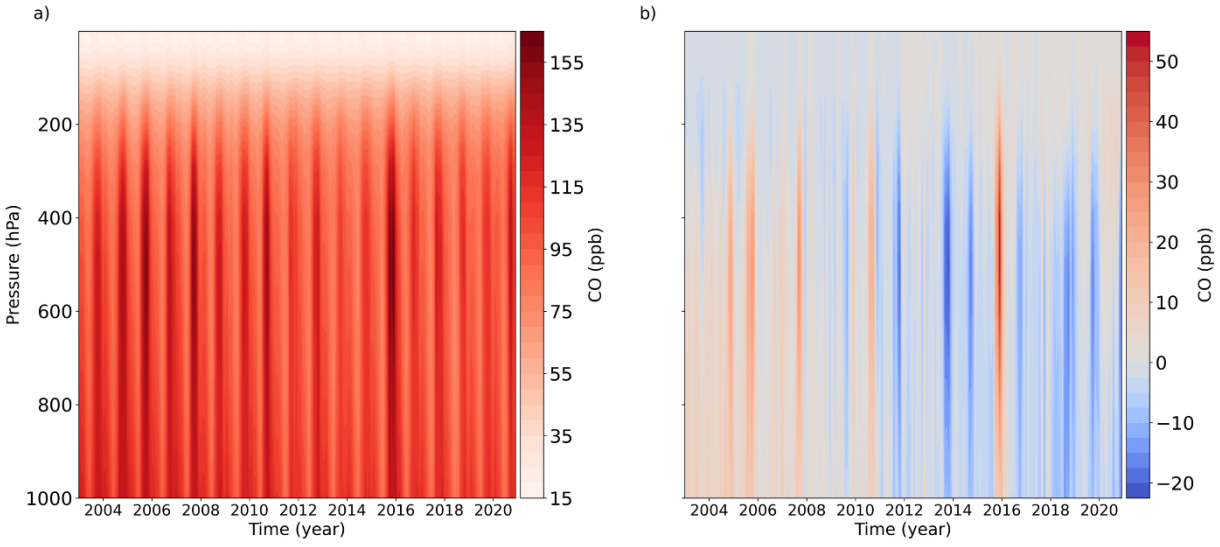

Figure 2 – Pressure *versus* time diagram for the (A) carbon monoxide time series; (B) carbon monoxide anomaly time series.

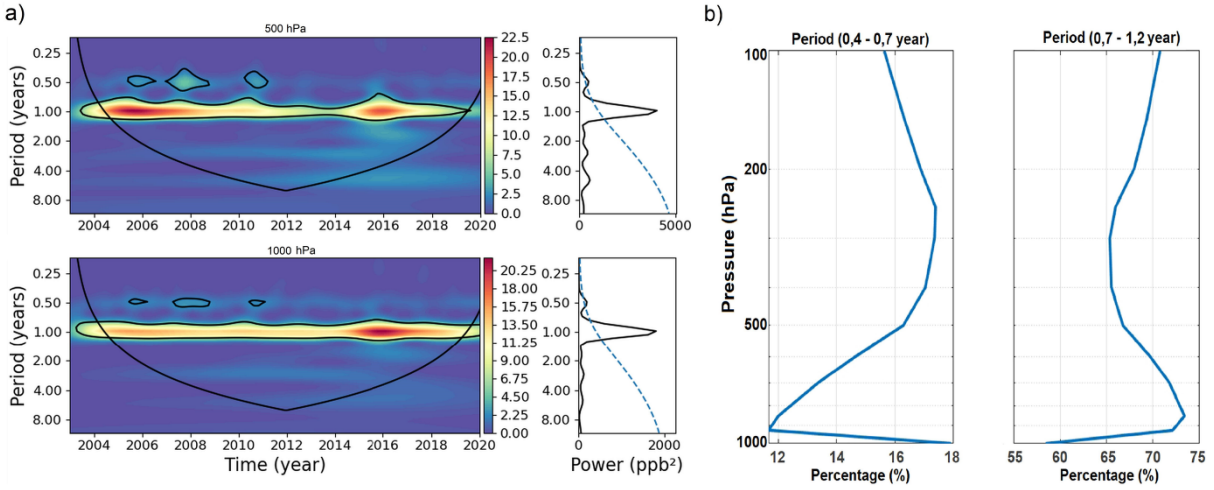

Figure 3 – (A) Local wavelet power spectrum (WPS) of the continuous wavelet transforms (CWT) of the CO concentration at 500 and 1,000 hPa over the Manaus Metropolitan Region, and global wavelet power (GWP). The U-shaped curve in the WPS graph indicates the influence cone and the continuous lines shows significant values at the 95% level. The dotted line in the global spectrum shows significance of 95%. (B) Vertical profiles of the variance percentage of the total variance of CO time series are explained by indicated scales.

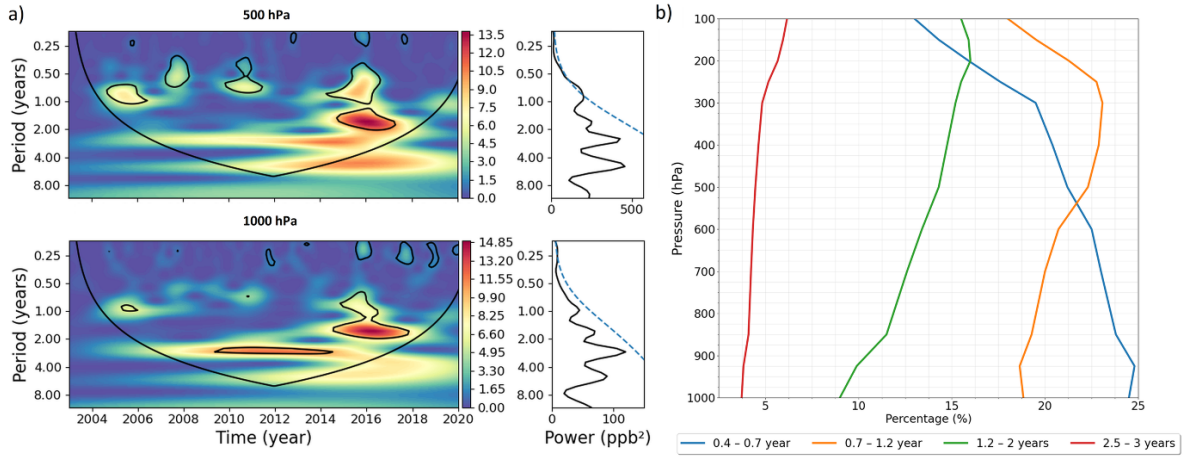

Figure 4 – (A) Local wavelet power spectrum (WPS) of the continuous wavelet transforms (CWT) of the CO anomalies over the Manaus Metropolitan Region at 500 and 1,000 hPa, and global wavelet power (GWP). The U-shaped curve in the WPS graph indicates the influence cone and the continuous lines shows significant values at the 95% level. The dotted line in the GWP shows significance of 95%. (B) Vertical profiles of the variance percentage of the total variance of CO anomaly time series explained by indicated scales.

Considering the time-frequency variations of the CO anomaly time series at 500 hPa obtained from the wavelet analysis, Figure 4A shows maximum variances on 0.5–1 year scale during the periods of 2004–2005, 2007, 2010–2012 and 2014–2017. Also, significant variance is observed for a 1.5–2 years scale in the 2014–2017 period. At 1,000 hPa level, significant variance is observed on the scales of 2.5–3 and 0.7–2 years, in the 2009–2014 and 2014–2017 periods, respectively. These results indicate that CO anomaly time series contains multiple variability scales, with dominance of the semiannual (0.4–0.7 year), annual (0.7–1.2 year) and interannual (1.2–2 and 2.5–3 years) scales. Figure 4B presents the average variance percentage profiles by scales in relation to the total variance of the anomaly time series. Semiannual scale represents between 13 and 24.5% of the variability contained in the total band, with the highest values found on surface levels; annual scale corresponds to approximately 18% at 1,000 hPa, and between 22 and 23% in the 500–200 hPa layer; 1.2–2 years scale varies between 9 and 16%, with higher variance values in the upper atmosphere, and, finally, 2.5–3 years scale represents about 4% of the variability near surface and 6% at upper layers. These four scales together represent about 55% of CO variability near the surface and approximately 63% at 500 hPa.

Relations between precipitation, fires and carbon monoxide

Figure 5A shows the WTC of CO concentration time series at 500 and 1,000 hPa levels using fire series as a reference. At the 500 hPa level, significant coherence occurs in the semiannual scale from 2004 to 2007 and subsequently from 2011 to 2017. The annual scale shows significant coherence throughout the period of analysis, with CO series lagging the fire series 1.5–2 months. After 2015, coherence extended to the 3 years scale, with the series oscillating in phase. Still in the 3 years scale, there is significant coherence between 2004 and 2010, with the series oscillating with phase difference of the 90º, that is, the maximum values in the CO series occurring nine months after the maximum of fire. At 1,000 hPa, significant coherence on the semiannual scale can be observed in 2006–2009, 2010–2017 and 2019, with the fire and CO series oscillating practically in-phase. In annual scale, coherence is significant throughout the analyzed period; however, the CO series shows a lag of around 3–6 months. Coherence is also observed on 3-year and 4.5 to 6 years scales throughout the analyzed period. For the anomaly series (Figure 5B), at 500 hPa, it is possible to note significant coherence in 0.2–0.4 years scale in several time intervals along the analyzed period. It is still possible to observe coherence in the annual scale for 2015 and 2016 years, with a phase difference of 1.5–3 months. After 2015, there is also coherence on the scales between 1.2 to 2.5 years, with a phase difference of 45º, that is around three months for periods up to two years, and with series oscillating in phase for the period of 2–3 years. At the 1,000 hPa level, significant coherence is observed for 2015 year on 0.3–0.8 and 1.2–1.8 year scales, both with a phase difference of 90º, that corresponds to a lag of approximately 1–3 months. Also, at this layer, significant coherence is observed for 3 years and 4.5 to 6 years scales throughout the entire period. These variability scales coincide with variability scales associated to ENSO, whose periodicity varies between three and seven years (Timmermann et al., 2018).

Complementary to the WTC analyses, the XWT analyses for fire and CO anomaly time series at 500 and 1,000 hPa are shown in Figure 5C. At 500 hPa, the series exhibit in-phase oscillations in the 0.7 year scale throughout 2005. Significant semiannual scales with a phase difference of approximately two months are observed in 2010 and 2011. Additionally, larger amplitudes in the 2.5–3 years scale can be seen from 2008 to 2015, with a brief interruption in 2013. Prior to 2013, the series exhibit the phase difference of the 90°, that corresponds to nine months, whereas after this year the time series oscillates in phase. Notably, in 2016, significant values in the XWT in 0.1–1 year and 1.2–2 years scales are observed, with phase differences of 90°, that correspond to 1.5–3 and 3 months, respectively.

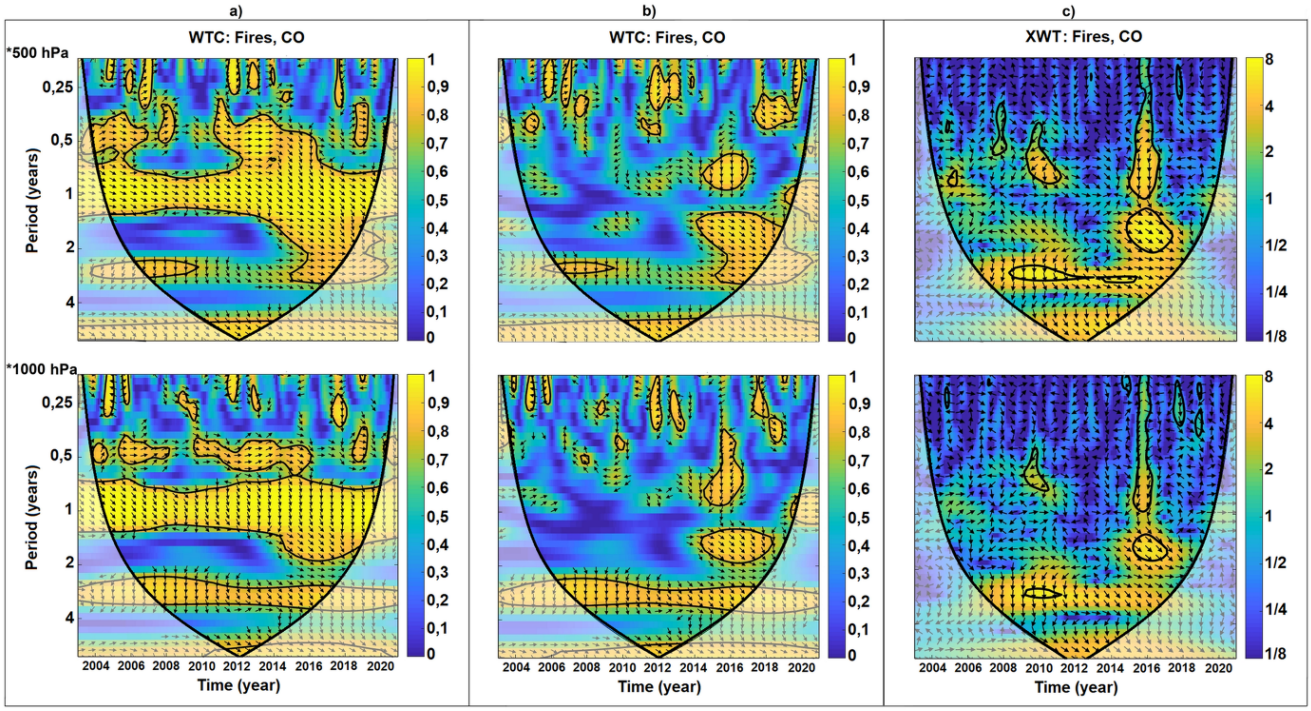

Figure 5 – The wavelet coherence and phase differences between fire and CO concentration at 500 and 1,000 hPa for (A) total monthly time series; (B) anomaly time series; (C) the cross-wavelet transform and phase differences between the fire anomaly and 500 and 1,000 hPa CO anomaly time series. The thick contour encompasses the significant coherences at the 95% confidence. The region where the edge effects are important is under the U-shape curve. Arrows are the phase differences with in-phase (0º), pointed to the right; antiphase (180º), pointed to the left; the first time series leading the second one by 90º, pointed downward; and the first time series lagging the second one by 90º, pointed upward.

At 1,000 hPa, significant values are observed in 2010 for periods of 0.5–0.7 years and 3 years scales. The former presents the phase difference of 180°, while the latter shows a phase difference of approximately 90° (nine months). In 2016, the same scales and phase difference are observed at 500 hPa.

Such results indicate that different mechanisms may be responsible for fires variability and, consequently, CO variability over the region. The relation between climate variability and the variability of fires was observed by analyzing the WTC spectrum in Figure 6A. In this figure, significant coherences are observed in 2005–10 and after 2015 for the 1–2, 2.5–3 and 4.5–6 years scales, with phase differences varying between 90° and 180°, indicating that a precipitation (PRP) series precedes a fire series, as shown in Figure 6B.

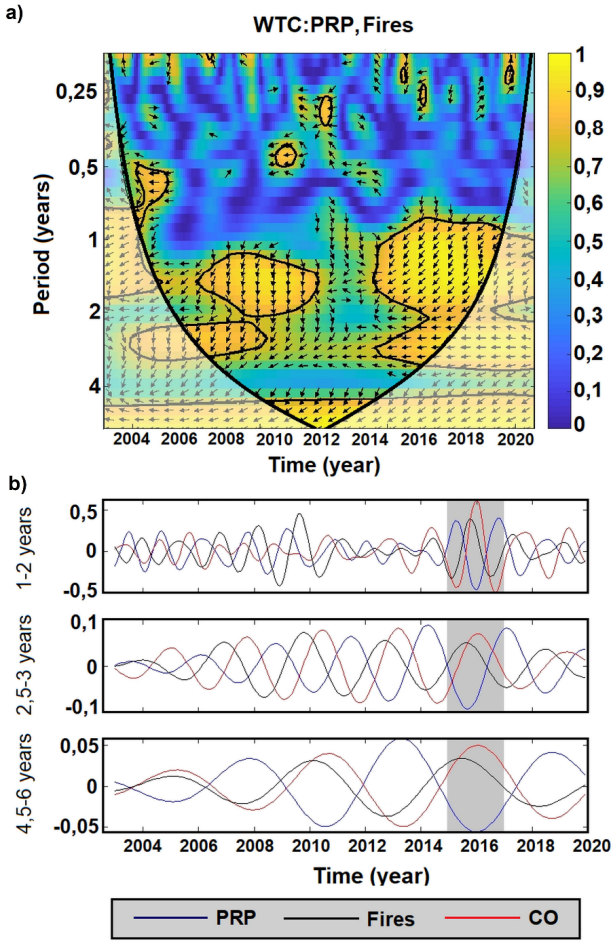

Figure 6 – (A) Wavelet coherence (WTC) between precipitation (PRP) and fire series. The thick contour encompasses the significant coherences at the 95% confidence. The region where the edge effects are important is under the U-shape curve. The arrows point out the phase differences, operating in the same way as shown in Figure 5. (B) Reconstructed CO, precipitation and fires anomaly time series for 1–2, 2.5–3 and 4.5–6 years scales. Highlighted, in gray, the period between 2015 and 2016.

Figure 6B shows the reconstructed precipitation, fires and CO anomaly time series for the three dominant variability scales, highlighting the period 2015–16, when an extreme positive CO concentration anomaly occurred. In this period, there is agreement between the series, with negative precipitation anomalies associated with an increase in fires and, consequently, in CO, which indicates that the interaction of climate variability modes in the different scales could play a differential role in the configuration and prolongation of rainfall events over the MMR that affect the fire distribution and CO concentration. So, climate variability modes should be analyzed separately for the mentioned timescales.

For these scales, different SST anomaly patterns were observed during the 2015–16 period. During the dry season (July–October/JASO) for the 1–2 years scale, positive SST anomalies in the eastern equatorial Pacific and negative in western equatorial Pacific define the El Niño pattern in 2015 (Figure 7A). Furthermore, in the tropical Indian Ocean, warming in the western sector accompanied by cooling in eastern sector defines an anomalous SST dipole pattern over this ocean. In the tropical Atlantic, cooling is observed along South America's north coast and over the eastern equatorial Atlantic. Associated with this SST anomaly pattern, negative rainfall anomalies were observed south of 10°S and in the northwestern Amazon (Figure 7C). During the wet season (November–March/NDJFM) (Figure 7B), positive SST anomalies related to El Niño show maximum values decoupled from South America coast, while the tropical Atlantic (Indian Ocean), the negative (positive) SST anomalies are weakened (intensified). Also, the warming in the tropical Atlantic occurs in the northwestern African coast. During this period, there is intensification of negative precipitation anomalies throughout the Amazon (Figure 7D).

For 2.5–3 years scale, during JASO, the El Niño pattern with anomalous warming in the eastern tropical Pacific is established, and negative SST anomalies are observed over the western equatorial Atlantic and southern tropical Atlantic along the African coast (Figure 7E). During NDJFM (Figure 7F), which includes the mature phase of the El Niño event, negative anomalies in the tropical Atlantic give way to a slight warming in the eastern equatorial Atlantic and along the southwest part of the southern tropical Atlantic. In this scale, El Niño acts to reduce rainfall across the basin; however, warming in the equatorial Atlantic acts in the opposite direction, causing precipitation anomalies to be slightly smaller in relation to the dry season (Figures 7G and 7H). The reconstructed SST anomalies on 4.5–6 years scale also configure a well-defined El Niño pattern in the eastern tropical Pacific during the two seasons (Figures 7I and 7J). However, for this scale, positive SST anomalies in the tropical Indian and tropical Atlantic Oceans occur simultaneously. El Niño, accompanied by the tropical Atlantic warming, were consistent with decreasing precipitation over the Amazon in both seasons. At this scale, the combined effect of El Niño and tropical north Atlantic warming acted to prolong the dry period to NDJFM, mainly at north of 10°S (Figures 7K and 7L).

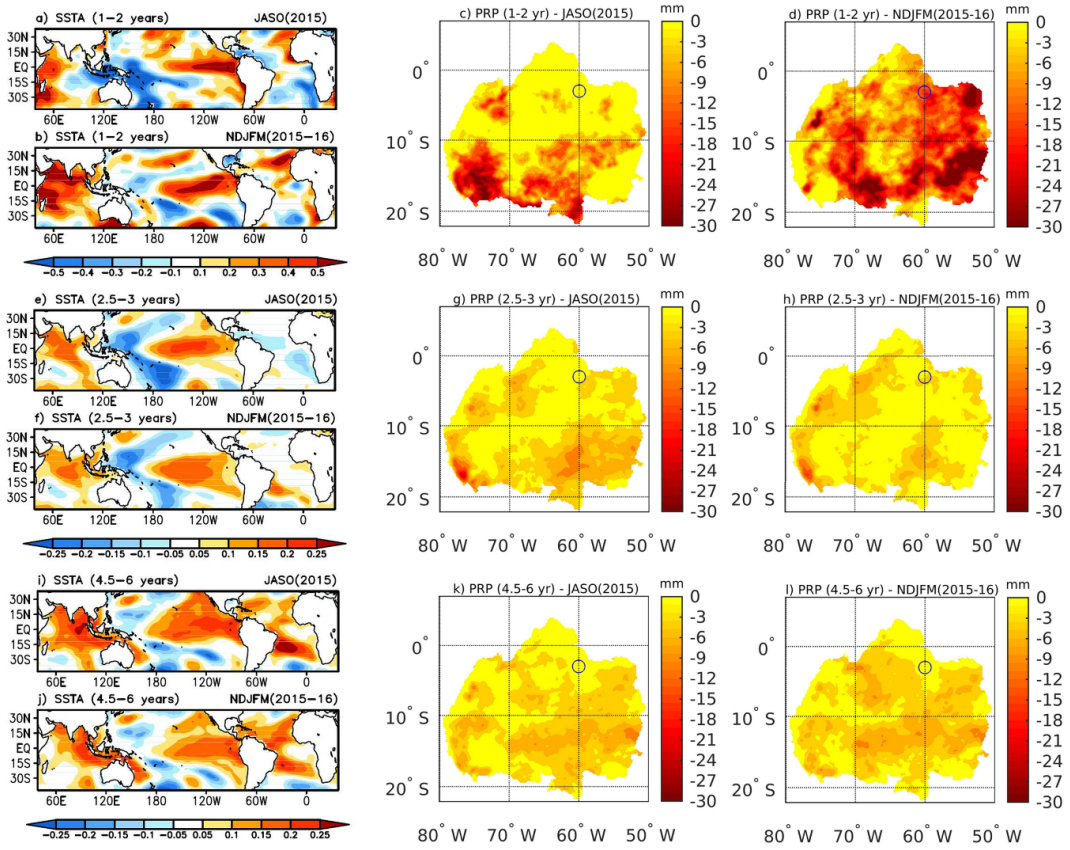

Figure 7 – Sea surface temperature anomalies reconstructed during, respectively, dry (JASO) and wet (NDJFM) seasons of 2015/16 for (A, B) 1–2, (E, F) 2.5–3 and (I, J) 4.5–6 years scales, and reconstructed rainfall anomalies over Amazon in dry (JASO) and wet (NDJFM) seasons of 2015/16 for (C, D) 1–2, (G, H) 2.5–3 and (K, L) 4.5–6 years scales.

Conclusion

The results presented here suggest that the seasonal behavior and interannual variability of the CO concentration over the MMR is controlled by fires and climate variability. It was found that semi-annual and annual cycles were responsible for up to 9% of the CO variability at near surface levels. When analyzing the CO anomaly time series, multiple scale variability between 0.4 to 3 years explains about 55% of the CO variability at 1,000 hPa and approximately 63% at 500 hPa. For the 3 year and 4.5–6 years scales, a strong relationship between the fire's variability and the variations in CO was observed for the period study. Since these scales coincide with the ENSO scale, the coherence analysis between precipitation and fires suggests that the dynamics of fires are partly associated with interannual climate variations, as discussed in previous studies (Aragão et al., 2018; Ribeiro et al., 2018a).

Therefore, analyzing the climate conditions during the extreme event in 2015–16, the results show that for the 1–2 years and 4.5–6 years scales both the tropical north Atlantic and the eastern equatorial Pacific affect the distribution of rainfall over the Amazon region, so that the increase in CO concentration is preceded by below normal rainfall conditions in this area occurring 1–3 months in advance. Furthermore, the results indicate that warming in the tropical north Atlantic occurring in phase with El Niño acts to intensify the negative precipitation anomalies during the region's rainy season. On the other hand, for the time scale of 2.5–3 years, the increase in CO is related to El Niño. In this case, the effect on precipitation was more intense during its development phase (JASO). The results here indicate that the influence of the tropical Pacific and the Atlantic on rainfall patterns over Amazon, and therefore on CO concentration during the 2015/16 dry season and dry-wet transition depends on the time scale of the variations. Specifically, in 2015/16, the combination of different scales contributed to the CO reaching higher values compared to previous years. Therefore, these results suggest that the interaction of climate variability modes in the different scales could play a differential role in the configuration and prolongation of rainfall events over the MMR that affect the fire distribution and CO concentration. These results show a new aspect of the importance of evaluating combined effects of climate variability in different scales on CO concentrations in the atmosphere, particularly during extreme events years.

Contribution of authors:

SIGNORI, R. T.: Conceptualization, Formal Analysis, Investigation, Methodology, Software, Visualization, Writing – original draft, Writing – review & editing. SOUZA, R. A. F.: Conceptualization, Data curation, Formal Analysis, Investigation, Methodology, Project administration, Software, Supervision, Visualization, Writing – review & editing. SOUZA, R. V. A.: Conceptualization, Data curation, Formal Analysis, Investigation, Methodology, Software, Supervision, Visualization, Writing – review & editing. RIBEIRO, I. O.: Writing – review & editing. KAYANO, M. T.: Writing – review & editing.

References

Aragão, L.E.O.C.; Anderson, L.O.; Fonseca, M.G.; Rosan, T.M.; Vedovato, L.B.; Wagner, F.H.; Silva, C.V.J.; Silva Junior, C.H.L.; Arai, E.; Aguiar, A.P.; Barlow, J.; Berenguer, E.; Deeter, M.N.; Domingues, L.G.; Gatti, L.; Gloor, M.; Malhi, Y.; Marengo, J.A.; Miller, J.B.; Phillips, O.L.; Saatchi, S., 2018. 21st Century drought-related fires counteract the decline of Amazon deforestation carbon emissions. Nature Communications, v. 9, (1), 536. https://doi.org/10.1038/s41467-017-02771-y.

Boian, C.; Kirchhoff, V.W.J.H., 2004. Measurements of CO in an aircraft experiment and their correlation with biomass burning and air mass origin in South America. Atmospheric Environment, v. 38, (37), 6337-6347. https://doi.org/10.1016/j.atmosenv.2004.08.021.

Climate Hazards Center, 2022. Climate Hazards Center InfraRed Precipitation with Station data (CHIRPS). (Accessed Jun. 2, 2022) at:. https://data.chc.ucsb.edu/products/CHIRPS-2.0/.

Davidson, E.A.; De Araüjo, A.C.; Artaxo, P.; Balch, J.K.; Brown, I.F.; Mercedes, M.M.; Coe, M.T.; Defries, R.S.; Keller, M.; Longo, M.; Munger, M.; Schroeder, J.W.; Soares-Filho, W.; Souza, B.S.; Wofsy, B.S., 2012. The Amazon basin in transition. Nature, v. 481, 321-328. https://doi.org/10.1038/nature10717.

Deeter, M.N.; Martínez-Alonso, S.; Andreae, M.O.; Schlager, H., 2018. Satellite-based analysis of CO seasonal and interannual variability over the Amazon Basin. Journal of Geophysical Research: Atmospheres, v. 123, (10), 5641-5656. https://doi.org/10.1029/2018JD028425.

Deeter, M.N.; Martínez-Alonso, S.; Gatti, L.V.; Gloor, M.; Miller, J.B.; Domingues, L.G.; Correia, C.S.C., 2016. Validation and analysis of MOPITT CO observations of the Amazon Basin. Atmospheric Measurement Techniques, v. 9, (8), 3999-4012. https://doi.org/10.5194/amt-9-3999-2016.

Erfanian, A.; Wang, G.; Fomenko, L., 2017. Unprecedented drought over tropical South America in 2016: significantly under-predicted by tropical SST. Scientific Reports, v. 7, (1), 5811. https://doi.org/10.1038/s41598-017-05373-2.

Fórum Nacional de Entidades Metropolitanas (FNEM), 2018. Região metropolitana de Manaus (AM) (Accessed Apr. 20, 2022) at:. https://fnembrasil.org/regiao-metropolitana-de-manaus-am/.

Funk, C.; Peterson, P.J.; Landsfeld, M.F.; Pedreros, D.H.; Verdin, J.P.; Rowland, J.D.; Romero, B.E.; Husak, G.; Michaelsen, J.; Verdin, A. P., 2014. A quasi-global precipitation time series for drought monitoring. US Geological Survey data series, v. 832, (4), 1-12. https://doi.org/10.3133/ds832.

Funk, C.; Peterson, P.J.; Landsfeld, M.F.; Pedreros, D.H.; Verdin, J.P; Shukla, S.; Husak, G.; Rowland, J.D.; Harrison, L.; Hoell, A.; Michaelsen, J., 2015. The climate hazards infrared precipitation with stations—a new environmental record for monitoring extremes. Scientific data, v. 2, (1), 150066. https://doi.org/10.1038/sdata.2015.66.

Grinsted, A.; Moore, J.C.; Jevrejeva, S., 2004. Application of the cross wavelet transform and wavelet coherence to geophysical time series. Nonlinear Processes in Geophysics, v. 11, (5-6), 561-566. https://doi.org/10.5194/npg-11-561-2004.

Hooghiemstra, P.B.; Krol, M.C.; van Leeuwen, T.T.; van der Werf, G.R.; Novelli, P.C.; Deeter, M.N.; Aben, I.; Röckmann, T., 2012. Interannual variability of carbon monoxide emission estimates over South America from 2006 to 2010. Journal of Geophysical Research, v. 117, (D15). https://doi.org/10.1029/2012JD017758.

Instituto Nacional de Pesquisas Espaciais (INPE), 2022. Monitoramento dos Focos Ativos por Região: BDQueimadas. INPE (Accessed Apr. 5, 2022) at:. https://queimadas.dgi.inpe.br/queimadas/portal-static/estatisticas_estados/.

Jiménez-Muñoz, J.C.; Mattar, C.; Barichivich, J.; Santamaría-Artigas, A.; Takahashi, K.; Malhi, Y.; Sobrino, J.A.; Schrier, G.V.D., 2016. Record-breaking warming and extreme drought in the Amazon rainforest during the course of El Niño 2015–2016. Scientific Reports, v. 6, (1), 33130. https://doi.org/10.1038/srep33130.

Kopacz, M.; Jacob, D.J.; Fisher, J.A.; Logan, J.A.; Zhang, L.; Megretskaia, I.A.; Yantosca, R.M.; Singh, K.; Henze, D.K.; Burrows, J.P.; Buchwitz, M.; Khlystova, I.; McMillan, W.W.; Gille, J.C.; Edwards, D.P.; Eldering, A.; Thouret, V.; Nedelec, P., 2010. Global estimates of CO sources with high resolution by adjoint inversion of multiple satellite datasets (MOPITT, AIRS, SCIAMACHY, TES). Atmospheric Chemistry and Physics, v. 10, (3), 855-876. https://doi.org/10.5194/acp-10-855-2010.

Langenfelds, R.L.; Francey, R.J.; Pak, B.C.; Steele, L.P.; Lloyd, J.; Trudinger, C.M.; Allison, C.E., 2002. Interannual growth rate variations of atmospheric CO2 and its δ13C, H2, CH4, and CO between 1992 and 1999 linked to biomass burning. Global Biogeochemical Cycles, v. 16, (3), 21-1-21-22. https://doi.org/10.1029/2001GB001466.

Lelieveld, J.; Gromov, S.; Pozzer, A.; Taraborrelli, D., 2016. Global tropospheric hydroxyl distribution, budget and reactivity. Atmospheric Chemistry and Physics, v. 16, (19), 12477-12493. https://doi.org/10.5194/acp-16-12477-2016.

Liu, J.; Logan, J.A.; Murray, L.T.; Pumphrey, H.C.; Schwartz, M.J.; Megretskaia, I.A., 2013. Transport analysis and source attribution of seasonal and interannual variability of CO in the tropical upper troposphere and lower stratosphere. Atmospheric Chemistry and Physics, v. 13, (1), 129-146. https://doi.org/10.5194/acp-13-129-2013.

Logan, J.A.; Prather, M.J.; Wofsy, S.C.; McElroy, M.B., 1981. Tropospheric chemistry: A global perspective. Journal of Geophysical Research: Oceans, v. 86, (C8), 7210-7254. https://doi.org/10.1029/JC086iC08p07210.

Marengo, J.A.; Nobre, C.A.; Tomasella, J.; Cardoso, M.F.; Oyama, M.D., 2008a. Hydro-climatic and ecological behaviour of the drought of Amazonia in 2005. Philosophical Transactions of the Royal Society B: Biological Sciences, v. 363, (1498), 1773-1778. https://doi.org/10.1098/rstb.2007.0015.

Marengo, J.A.; Nobre, C.A.; Tomasella, J.; Oyama, M.D.; De Oliveira, G.S.; De Oliveira, R.; Camargo, H.; Alves, L.M.; Brown, I.F., 2008b. The drought of Amazonia in 2005. Journal of Climate, v. 21, (3), 495-516. https://doi.org/10.1175/2007JCLI1600.1.

Marengo, J.A.; Tomasella, J.; Alves, L.M.; Soares, W.R.; Rodriguez, D.A., 2011. The drought of 2010 in the context of historical droughts in the

Amazon region. Geophysical Research Letters, v. 38, (12). https://doi.org/10.1029/2011GL047436.

McMillan, W.W.; Evans, K.D.; Barnet, C.D.; Maddy, E.S.; Sachse, G.W.; Diskin, G.S., 2011. Validating the AIRS Version 5 CO retrieval with DACOM in situ measurements during INTEX-A and-B. IEEE Transactions on Geoscience and Remote Sensing, v. 49, (7), 2802-2813. https://doi.org/10.1109/TGRS.2011.2106505.

National Oceanic Atmospheric and Administration (NOAA), 2022. Historical El Niño / La Niña episodes (1950-present). NOAA (Accessed Jun. 16, 2022) at:. https://origin.cpc.ncep.noaa.gov/products/analysis_monitoring/ensostuff/ONI_v5.php.

Novelli, P.C.; Masarie, K.A.; Lang, P.M.; Hall, B.D.; Myers, R.C.; Elkins, J.W., 2003. Reanalysis of tropospheric CO trends: Effects of the 1997–1998 wildfires. Journal of Geophysical Research: Atmospheres, v. 108, (D15). https://doi.org/10.1029/2002JD003031.

Panisset, J.S.; Libonati, R.; Gouveia, C.M.P.; Machado-Silva, F.; França, D.A.; França, J.R.A.; Peres, L.F., 2018. Contrasting patterns of the extreme drought episodes of 2005, 2010 and 2015 in the Amazon Basin. International Journal of Climatology, v. 38, (2), 1096-1104. https://doi.org/10.1002/joc.5224.

Petrenko, V.V.; Martinerie, P.; Novelli, P.; Etheridge, D.M.; Levin, I.; Wang, Z.; Blunier, T.; Chappellaz, J.; Kaiser, J.; Lang, P.; Steele, L.P.; Hammer, S.; Mak, J.; Langenfelds, R.L.; Schwander, J.; Severinghaus, J.P.; Witrant, E.; Petron, G.; Battle, M.O.; Forster, G.; Sturges, W.T.; Lamarque, J.-F.; Steffen, K.; White, J.W.C., 2013. A 60 yr record of atmospheric carbon monoxide reconstructed from Greenland firn air. Atmospheric Chemistry and Physics, v. 13, (15), 7567-7585. https://doi.org/10.5194/acp-13-7567-2013.

Ribeiro, I.O.; Andreoli, R.V.; Kayano, M.T.; Sousa, T.R.; Medeiros, A.S.; Godoi, R.H.M.; Godoi, A.F.L; Duvoisin, S.J.; Martin, S.T.; de Souza, R.A.F., 2018a. Biomass burning and carbon monoxide patterns in Brazil during the extreme drought years of 2005, 2010, and 2015. Environmental Pollution, v. 243, (part B), 1008-1014. https://doi.org/10.1016/j.envpol.2018.09.022.

Ribeiro, I.O.; Andreoli, R.V.; Kayano, M.T.; Sousa, T.R.; Medeiros, A.S.; Guimarães, P.C.; Barbosa, C.G.G.; Godoi, R.H.M.; Martin, S.T.; de Souza, R.A.F., 2018b. Impact of the biomass burning on methane variability during dry years in the Amazon measured from an aircraft and the AIRS sensor. Science of The Total Environment, v. 624, 509-516. https://doi.org/10.1016/j.scitotenv.2017.12.147.

Ribeiro, I.O.; Santos, E.O.; Batista, C.E.; Fernandes, K.S.; Ye, J.; Medeiros, A.S.; de Oliveira, R.L.; de Sá, S.S.; de Sousa, T.R.; Kayano, M.T.; Andreoli, R.V.; Machado, C.M.D.; Surratt, J.D.; Junior, S.D.; Martin, S.T.; de Souza, R.A.F., 2020. Impact of biomass burning on a metropolitan area in the Amazon during the 2015 El Niño: The enhancement of carbon monoxide and levoglucosan concentrations. Environmental Pollution, v. 260, 114029. https://doi.org/10.1016/j.envpol.2020.114029.

Rozante, J.R.; Rozante, V.; Alvim, D.S.; Manzi, A.O.; Chiquetto, J.B.; D'Amelio, M.T.S.; Moreira, D.S., 2017. Variations of carbon monoxide concentrations in the megacity of São Paulo from 2000 to 2015 in different time scales. Atmosphere, v. 8, (5), 81. https://doi.org/10.3390/atmos8050081.

Santos, Y.L.F.D.; Souza, R.A.F.D.; Souza, J.M.D.; Andreoli, R.V.; Kayano, M.T.; Ribeiro, I.O.; Guimarães, P.C., 2017. Variabilidade espaço-temporal do monóxido de carbono sobre a América do Sul a partir de dados de satélite de 2003 a 2012. Revista Brasileira de Meteorologia, v. 32, (1), 89-98. https://doi.org/10.1590/0102-778632120150163.

Seiler, W.; Giehl, H.; Brunke, E.G.; Halliday, E., 1984. The seasonality of CO abundance in the Southern Hemisphere. Tellus B, v. 36, (4), 219-231. https://doi.org/10.3402/tellusb.v36i4.14906.

Shindell, D.T.; Faluvegi, G.; Koch, D.M.; Schmidt, G.A.; Unger, N.; Bauer, S.E., 2009. Improved attribution of climate forcing to emissions. Science, v. 326, (5953), 716-718. https://doi.org/10.1126/science.1174760.

Strode, S.A.; Duncan, B.N.; Yegorova, E.A.; Kouatchou, J.; Ziemke, J.R.; Douglass, A.R., 2015. Implications of carbon monoxide bias for methane lifetime and atmospheric composition in chemistry climate models. Atmospheric Chemistry and Physics, v. 15, (20), 11789-11805. https://doi.org/10.5194/acp-15-11789-2015.

Timmermann, A.; An, S.I.; Kug, J.S.; Jin, F.F.; Cai, W.; Capotondi, A.; Cobb, K.; Lengaigne, M.; McPhaden, M.J.; Stuecker, M.F.; Stein, K.; Wittenberg, A.T.; Yun, K.S.; Bayr, T.; Chen, H.C.; Chikamoto, Y.; Dewitte, B.; Dommenget, D.; Grothe, P.; Guilyardi, E.; Ham, Y.G.; Hayashi, M.; Ineson, S.; Kang, D.; Kim, S.; Kim, W.; Lee, J.Y.; Li, T.; Luo, J.J.; McGregor, S.; Planton, Y.; Power, S.; Rashid, H.; Ren, H.L.; Santoso, A.; Takahashi, K.; Todd, A.; Wang, G.; Wang, G.; Xie, R.; Yang, W.H.; Yeh, S.W.; Yoon, J.; Zeller, E.; Zhang, X., 2018. El Niño–southern oscillation complexity. Nature, v. 559, (7715), 535-545. https://doi.org/10.1038/s41586-018-0252-6.

Torrence, C.; Compo, G.P., 1998. A practical guide to wavelet analysis. Bulletin of the American Meteorological Society, v. 79, (1), 61-78. https://doi.org/10.1175/1520-0477(1998)079≤0061:APGTWA≥2.0.CO;2.

Torrence, C.; Webster, P.J., 1999. Interdecadal changes in the ENSO–monsoon system. Journal of climate, v. 12, (8), 2679-2690. https://doi.org/10.1175/1520-0442(1999)012≤2679:ICITEM≥2.0.CO;2.

Vale, R.S.; Santana, R.A.; Júnior, C.Q.D., 2020. Análise de dados climáticos usando transformada em ondeletas cruzada e coerência. Revista Brasileira de Geografia Física, v. 13, (2), 641-647. https://doi.org/10.26848/rbgf.v13.2.p641-647.

van der Werf, G.R.; Randerson, J.T.; Giglio, L.; Collatz, G.J.; Mu, M.; Kasibhatla, P.S.; Morton, D.C.; DeFries, R.S.; Jin,Y.; van Leeuwen, T.T., 2010. Global fire emissions and the contribution of deforestation, savanna, forest, agricultural, and peat fires (1997–2009). Atmospheric Chemistry and Physics, v. 10, (23), 11707-11735. https://doi.org/10.5194/acp-10-11707-2010.

van Marle, M.J.E.; Field, R.D.; van der Werf, G.R.; Estrada de Wagt, I.A.; Houghton, R.A.; Rizzo, L.V.; Artaxo, P.; Tsigaridis, K., 2017. Fire and deforestation dynamics in Amazonia (1973–2014). Global Biogeochemical Cycles, v. 31, (1), 24-38. https://doi.org/10.1002/2016GB005445.

Weng, H.; Lau, K.M., 1994. Wavelets, period doubling, and time–frequency localization with application to organization of convection over the tropical western Pacific. Journal of Atmospheric Sciences, v. 51, (17), 2523-2541. https://doi.org/10.1175/1520-0469(1994)051≤2523:WPDATL≥2.0.CO;2.

Worden, H.M.; Deeter, M.N.; Edwards, D.P.; Gille, J.C.; Drummond, J.R.; Nédélec, P., 2010. Observations of near-surface carbon monoxide from space using MOPITT multispectral retrievals. Journal of Geophysical Research: Atmospheres, v. 115, (D18). https://doi.org/10.1029/2010JD014242.

Yashiro, H.; Sugawara, S.; Sudo, K.; Aoki, S.; Nakazawa, T., 2009. Temporal and spatial variations of carbon monoxide over the western part of the Pacific Ocean. Journal of Geophysical Research: Atmospheres, v. 114, (D8). https://doi.org/10.1029/2008JD010876.

Zhang, L.; Jiang, H.; Lu, X.; Jin, J., 2016. Comparison analysis of global carbon monoxide concentration derived from SCIAMACHY, AIRS, and MOPITT. International Journal of Remote Sensing, v. 37, (21), 5155-5175. https://doi.org/10.1080/01431161.2016.1230282.

Zheng, B.; Chevallier, F.; Yin, Y.; Ciais, P.; Fortems-Cheiney, A.; Deeter, M.N.; Parker, R.J.; Wang, Y.; Worden, H.M.; Zhao, Y., 2019. Global atmospheric carbon monoxide budget 2000–2017 inferred from multi-species atmospheric inversions. Earth System Science Data, v. 11, (3), 1411-1436. https://doi.org/10.5194/essd-11-1411-2019.